



Promoting the activity of Ce-incorporated MOR in dimethyl ether carbonylation through tailoring the distribution of Brønsted acids

Ying Li^a, Shouying Huang^{a,*}, Zaizhe Cheng^a, Kai Cai^a, Landong Li^b, Emile Milan^c, Jing Lv^a, Yue Wang^a, Qi Sun^a, Xinbin Ma^{a,*}



^a Key Laboratory for Green Chemical Technology of Ministry of Education, Collaborative Innovation Center of Chemical Science and Engineering, School of Chemical Engineering and Technology, Tianjin University, Tianjin 300350, China

^b School of Materials Science and Engineering & National Institute for Advanced Materials, Nankai University, Tianjin 300350, China

^c School of Information Technology and Engineering, University of Ottawa, 800 King Edward Avenue, Ottawa, ON, Canada

ARTICLE INFO

Keywords:

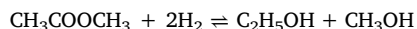
H-MOR
Heteroatom substitution
Al sitting
Brønsted acid site distribution
Carbonylation reaction

ABSTRACT

As Brønsted acid site (BAS) located in 8-membered ring (8-MR) of zeolite is accepted as the exclusive active site for dimethyl ether carbonylation to methyl acetate, tailoring the distribution of tetrahedral Al in zeolite channels is important to improve catalytic performance. In this work, a series of Ce-containing mordenite were synthesized by one-step hydrothermal method. By a combination of mutually complementary characterization techniques (e.g. XPS, UV-vis, Raman, acidity characterizations etc.), it is confirmed that Ce atoms incorporated into the zeolite framework as Ce³⁺ species, resulting in an enrichment of BAS in the 8-MR. Acid strength, apparent activation energy and DFT calculations revealed that the incorporation of Ce resulted in an increase of Si–OH–Al in the 8-MR, which was responsible for the improved activity. This work provides a facile way to tailor the acidic concentration and distribution of zeolites, which is able to guide rational design of zeolites for the shape-selective catalysis.

1. Introduction

Growing concerns about environment, depletion of oil reserves, and energy security have pushed the topic of energy to the center stage. In order to reduce the reliance on imported crude oil, searching for alternatives to petroleum-derived fuels and chemicals for many countries has gained momentum in past decades. In the context, ethanol as a potential alternative synthetic fuel has attracted tremendous interests [1–3]. Recently, a new route of ethanol production has been developed, which relies on transformation of the carbon source (such as coal, biomass) into syngas [4–7]. This process is an integrated technology consisting of carbonylation of dimethyl ether (DME) to form methyl acetate (MA) and the subsequent hydrogenation to yield ethanol (Eqs. (1) and (2)), both of which shows appreciable selectivity. The main byproduct methanol can be recycled to produce DME by dehydration. Furthermore, the absence of ethanol-water binary azeotrope in products significantly reduces separation cost. Therefore, the advantages of high atom economy, low energy consumption and few emissions make this route promising and competitive in industry.



As a key step in conversion of syngas to ethanol, the carbonylation of DME to MA is usually catalysed by solid acid catalysts such as zeolites and heteropoly acids (HPAs) [8–10]. Compared with HPAs, zeolites show favourable activity and selectivity due to confinement effect of well-defined structure. Zeolite catalyzed DME carbonylation reaction is proved to be a typical spatially confined reaction on Brønsted acid sites [5,10,11]. The catalytic performance strongly depends on the structure of zeolite framework and the distribution of Brønsted acid site [12,13]. Mordenite (MOR) has been demonstrated as an outstanding candidate to catalyze this reaction, which contains a main channel with 12-membered ring (12-MR, 6.7 × 7.0 Å) along the [0 0 1] direction and an 8-membered ring side pockets (8-MR, 3.4 × 4.8 Å) in the [0 1 0] direction [14]. The 8-MR channels that surround catalytically active Brønsted acid sites confine reactive intermediates in dimensions, imparting shape-selective properties that facilitate MA formation. In contrast, the 12-MR with larger voids is prone to the coke deposit [15–17]. Therefore, it is anticipated that modulating the distribution of framework Al to selectively concentrating the Brønsted acid site within 8-MR is an efficient strategy to improve the yield of MA, even if it is still

* Corresponding authors.

E-mail addresses: huangs@tju.edu.cn (S. Huang), xbma@tju.edu.cn (X. Ma).

a quite challenging task.

To date, several approaches have aimed at tailoring the Brønsted acidity in aluminosilicate zeolite. Post-synthesis modifications in acidic/alkaline media or steam are extensively investigated for introducing or removing tetrahedral AlO_4 units to modify the acidity [18–20]. However, they tend to give rise to associated drawbacks, such as the deterioration of crystallinity, the blockage of channels and the shield of acid sites. Modification of hydrothermal synthesis by manipulating Si and Al composition and choosing an appropriate organic structure directing agent are also capable to induce non-random distribution of framework Al (Al_F) atoms [21–24]. Recently, growing interest is focused on the heteroatom-substitution during one-pot synthesis [25–28]. Compared with the above two methods, it is an effective and controllable way to adjust the Brønsted acid site location corresponding to Al_F siting. Because dislodgement of Al_F atoms among different channels may occur by virtue of the competitive occupancy between Al_F and the heteroatom. Furthermore, the heteroatom composition (e.g. Ga^{3+} , Fe^{3+} , and B^{3+}) influences the acid strength [29,30], which plays an important role in the catalytic properties.

In this work, we reported a facile protocol for deliberately regulating H-MOR acidity by heteroatom isomorphous substitution. A series of Ce-containing MOR zeolites were successfully synthesized by one-step hydrothermal method. We endeavored to explore the nature of Ce species as well as the evidence of changes in acidity of the Ce-doped MOR by several complementary characterization techniques. Afterwards, DFT calculations and catalytic evaluations were combined to elucidate the promotion mechanism of Ce modified MOR catalysts.

2. Experimental

2.1. Synthesis of Ce-incorporated MOR zeolites

The Ce-containing MOR zeolites were synthesized by implementing a one-pot hydrothermal method. The synthesis process as well as key factors in preparation was diagrammatically represented in Fig. S1. Silica source (30 wt.% SiO_2), NaAlO_2 , NaOH and $\text{Ce}(\text{NO}_3)_3$ were mixed and stirred at room temperature for 4 h, followed by adding tetraethylammonium hydroxide (TEAOH, 25 wt.%, Guangfu Fine Chemical Co., Ltd.) aqueous solution as the structure-directing agent and commercial MOR (Nankai University catalyst Co., Ltd.) as the seed (1 wt.% relative to SiO_2). The molar composition of the synthesis gel was $1.0\text{SiO}_2 \cdot 0.083\text{NaAlO}_2 \cdot 0.2\text{NaOH} \cdot 0.23\text{TEAOH} \cdot n\text{Ce}(\text{NO}_3)_3$ ($n = 0, 0.01, 0.021, 0.042$). The well-mixed gel was stirred for 1.5 h and then crystallized in a Teflon-lined stainless steel autoclave at 170 °C for 3 days. After the reaction, the autoclave was cooled down and the products were filtered, washed with deionized water, dried overnight at 100 °C and calcinated at 550 °C. The temperature for calcination was increased with a ramp of 1 °C/min from room temperature to 550 °C, then maintained at 550 °C for 5 h, aiming to remove the structure-directing agent completely. The detemplated samples were ion-exchanged with NH_4NO_3 (0.2 M) twice at 80 °C for 6 h, then dried overnight at 100 °C, followed by calcination at 500 °C for 4 h with a heating rate of 2 °C/min. The obtained zeolites were denoted as $x\text{Ce}-\text{M}$, where x represented the mole percentage of Ce in sum of Ce, Al and Si in the samples determined by ICP-OES.

For reference, a Ce-containing MOR sample was prepared by physical mixing process (see procedure in Fig. S1). The 0Ce-M and $\text{Ce}(\text{NO}_3)_3$ mixture was milled in a planetary ball mill for 10 h at 160 r/min, and then calcined at 500 °C for 4 h. The prepared sample was labelled as $y\text{Ce}/\text{M}$, where y represented the mole percentage of Ce in sum of Ce, Al and Si in the sample. Furthermore, another sample without Ce was prepared and labeled as 0Ce-M-BM. The preparation was similar to $y\text{Ce}/\text{M}$ but without the addition of $\text{Ce}(\text{NO}_3)_3$.

2.2. Catalytic evaluations

The reactions of DME carbonylation to MA were performed in a stainless-steel tubular fixed-bed reactor (8.0 mm i.d.) under 1.5 MPa. Typically, 1 ml of catalyst (~0.5 g, 40–60 mesh) was loaded and pretreated under N_2 atmosphere (99.99%, Tianjin Sixon Gas Co., Ltd) at 200 °C for 9 h. The catalytic reaction was initiated by introducing the reactant gases (DME/CO = 1:49, vol.: vol.) with a constant flow rate of 100 ml/min adjusted by a mass flow controller. The reaction conditions (i.e. pressure, ratio of DME/CO) were chosen in accordance with the previously reported optimized system [7,16]. The products were analysed by a gas chromatograph (Agilent 7890B) equipped with a flame ionization detector (FID) and a thermal conductivity detector (TCD). The conversion of DME (X_{DME}), selectivity of MA (S_{MA}) and the space time yield of MA (MA STY) were calculated by using the equations in previous study [31,32]. TOF was calculated on the following equation:

$$\text{TOF(h}^{-1}\text{)} = \frac{\text{Total flow rate of DME (mol/h)} \times X_{\text{DME}}}{m_{\text{cat}}(\text{g}) \times \text{Number of Brønsted acid site in 8-MR (mol/g)}}$$

2.3. Characterization

X-ray diffraction (XRD) measurement were carried out using a Rigaku D/max-2500 diffractometer with $\text{Cu K}\alpha$ radiation ($\lambda = 1.54056 \text{ \AA}$), operating at 40 kV and 200 mA. The patterns were collected in the range of $2\theta = 3^\circ\text{--}50^\circ$ with a scanning speed of 8°/min.

The actual atomic composition of $x\text{Ce}-\text{M}$ zeolites was determined by inductively coupled plasma optical emission spectrometry (ICP-OES) (VISTA-MPX, Varian).

Nitrogen adsorption was performed at –196 °C on a Micrometrics ASAP 2020 instrument to evaluate the textual properties of the catalyst. Prior to conducting the analysis, the samples were outgassed under high vacuum conditions at 200 °C for 24 h in order to remove adsorbed species such as water. The total pore volumes and median pore width were determined by Horvath-Kawazoe (H-K) equation. The micropore surface area and the micropore volume were calculated using the t-plot method.

Diffuse reflectance ultraviolet-visible (UV-vis) spectra were collected using a Shimazu UV-2550 UV-vis spectrophotometer in the range of 200 nm–600 nm with BaSO_4 as a reference.

X-ray photoelectron spectroscopy (XPS) was performed by employing a Thermo Fisher ESCALAB 250Xi instrument using monochromatic $\text{Al K}\alpha$ source ($h\nu = 1486.6 \text{ eV}$) as an X-ray source. Prior to the analysis, the samples were dried at 110 °C for 4 h to remove water and other adsorbed species. An operating power of 150 W and a pass energy of 30.0 eV were applied to scan the energy region of the photoelectrons. All binding energies were calibrated internally by the C1s peak at 284.8 eV. The number of scans for O 1s and Ce 3d are 2 and 8, respectively.

^{27}Al magic-angle spinning nuclear magnetic resonance (^{27}Al MAS NMR) spectra of samples were recorded using a Varian Infinityplus 300 MHz spectrometer operating at a magnetic field of 7.0 T magnet. The experiments were performed at 78.1 MHz using a 4 mm MAS probe at a rate of 8 kHz. The spectra were acquired at ambient temperature from 512 scans with a $\pi/12$ pulse width of 0.6 us and a recycle delay of 3 s. Chemical shifts were referenced versus excess aluminium nitrate aqueous solution.

^{29}Si MAS NMR investigations were recorded by a Bruker Avance III 400WB spectrometer using a 7 mm probe at resonance frequencies of 79.5 MHz. The spectra were measured upon single pulse excitation of $\pi/2$ for ^{29}Si with repetition time of 20 s and recorded with sample spinning rate of 4 kHz.

The Fourier transform infrared (FTIR) spectra in the region of framework T–O–T vibration were recorded using a Thermo Scientific Nicolet 6700 apparatus equipped with a DTGS detector. Each spectrum was obtained by averaging 32 scans collected at 4 cm^{-1} resolution using KBr as diluent (1 mg sample / 100 mg KBr).

The FTIR spectra of O–H region were recorded a mercury cadmium telluride (MCT) detector. In each experiment, a self-supported wafer (13 mm dia.) made of 20 mg of catalyst was loaded into the *in situ* stainless steel cell equipped with CaF₂ windows and connected to an evacuation system. The catalyst wafer was degassed under a vacuum of 10⁻⁴ Pa and heated at 400 °C for 1 h to completely remove the impurities from the surface of samples. The spectra were obtained at 30 °C at a resolution of 4 cm⁻¹ by averaging 32 scans. All the FTIR spectra were normalized by the weight of the wafers.

The Raman spectra were taken on a HR Evolution confocal Raman microscope system (HORIBA, France). A 266 nm laser with an X 50 air objective was employed. The Raman signal was acquired using a 2400 lines/mm grating centered between 200 and 1800 cm⁻¹. For each spectrum, the acquisition time were 120 s.

NH₃-TPD experiment was conducted using a Micromeritics Autochem II 2920 instrument equipped with a TCD. In a typical test, 100 mg of the catalyst was loaded in a quartz tube and cleaned by flowing Ar at a rate of 10 ml/min for 1 h at 200 °C. Then the sample was exposed to excess NH₃, followed by purging with Ar for 1 h at 30 ml/min to remove the physically adsorbed NH₃. The TPD profiles were recorded from 150 °C to 850 °C at a rate of 10 °C/min under a He flow (30 mL/min).

In situ FTIR spectra of alkaline probe molecules (pyridine and NH₃) adsorption were recorded to quantify the number of Brønsted acid sites in different channels. The background spectrum was collected when the sample was cooled to 150 °C in vacuum. Subsequently, the catalyst was saturated with pyridine or NH₃ for 30 min, and then evacuated to eliminate physically adsorbed molecules. IR spectra were collected in the range of 4000–1100 cm⁻¹ at a resolution of 4 cm⁻¹ by averaging 32 scans.

TPD-IR of NH₃ after pyridine saturation was collected on the same facility to exclusively determine the acidic strength of Brønsted acid sites in 8-MR channels. After being saturated by pyridine vapor, the self-supported wafer was exposed to 10% NH₃/Ar at 150 °C for 30 min, and outgassed in order to remove excess NH₃ in gas phase as well as physisorbed species. Subsequently, the sample was heated at a ramp rate of 10 °C/min to 600 °C under the vacuum condition to allow NH₃ and pyridine desorption, and the spectra were acquired at every 3.3 °C. The differential change of IR intensity with respect to temperature, which originates from desorption of NH₃ within Brønsted acid sites in 8-MR, was calculated based on the intensity of band at 1427 cm⁻¹, and the negative value -d(I_{1427 cm⁻¹})/dT reflected the desorption rate of NH₃ [33].

2.4. Computational details

Density functional theory (DFT) calculations were performed by using the double numeric quality basis set plus polarization (DNP) implemented in the Dmol³ program package. The Perdew Wang (PW91) functional was employed throughout all computations. Considering to computational efforts, the core electrons of Ce and Al atoms were replaced by an effect core potentials (ECP) while other atoms were treated in an all-electron basis set. The convergence tolerance of energy, maximum force and maximum displacement were 2 × 10⁻⁵ Ha, 4 × 10⁻³ Ha/Å and 5 × 10⁻³ Å, respectively. The complete linear synchronous transit (LST) and quadratic synchronous transit (QST) approach were employed to determine the transition state (TS). All the TSs were verified by only one imaginary frequency.

The MOR framework consists of two channels: a large 12-MR and an 8-MR side pocket. The two channels interconnect vertically with each other. In the MOR framework, there are four nonequivalent tetrahedral sites: T2 and T4 sites in the main channel, T3 in the 8-MR and T1 in the network between the 8-MR and 12-MR channels. In this study, a cluster model consisting of 100 tetrahedral sites (shown in Fig. 1a) extracted from the periodic MOR structure was employed to determine the preferred location of Ce³⁺ and Al³⁺ in MOR. The acidity of Brønsted acid

sites on T3AlO33H and T3CeO33H and the corresponding activation energies for CO insertion (rate-determining step) were also obtained on the 100 tetrahedral sites structure (100 T) (Fig. 1a–c). The acidity and activation energy of O–H in T3AlO33H and T3CeO33H were also obtained based on the 100 tetrahedral sites structure (100 T) (Fig. 1a–c). Note that the adopted model was large enough to enclose the main channel (12-MR) and the side pocket (8-MR) at the center of the structure so as to ensure greater accuracy in DFT calculations. The substitution energies of Si⁴⁺ by Al³⁺ (E_{subAl}) of the sites around the T1 were calculated based on a 62 tetrahedral sites (62 T) structure with T1 site in the center (Fig. 1e–f). All the next-nearest-neighbor T-sites of T1 were considered. In order to ensure that the local environment of Ce³⁺ and Al³⁺ center could provide reasonable information, all of the considered substitution sites were at least linked to four –O–(SiO₃)₃ groups. The structure was terminated by H atoms located 1.11 Å from the O atoms and orientated toward the Si atoms in the next coordination sphere.

The deprotonation energy (DPE) is defined as the energy required to break the H–O bond on zeolite framework, forming a proton and a zeolite framework anion. An acid site with a large DPE value corresponds to weak acidity. The DPE was calculated using the following formula:

$$E_{DPE} = E_{ZeO^-} - E_{ZeO-H}$$

where E_{ZeO⁻} refers to the energy of the zeolite framework without the H⁺ and E_{ZeO-H} is the energy of a neutral zeolite with Brønsted acid sites.

The substitution energies of Si by Al (E_{subAl}) were calculated according to the following equation:

$$E_{subAl} = E_{ZeO-Al3+} + E_{Si(OH)4} - E_{ZeO-Si4+} - E_{Al(OH)3} - E_{H2O}$$

where E_{ZeO-Al3+} and E_{ZeO-Si4+} are the energies of MOR zeolite after and before Si atom is substituted by heteroatom, respectively. E_{Si(OH)4}, E_{Al(OH)3} and E_{H2O} are energies of corresponding molecules. A lower value of E_{subAl} suggests the substitution of Si is preferable.

The E_{subAl} difference between T1 site occupied by Al³⁺ and Ce³⁺ (ΔE_{subAl(T1Al-T1Ce)}) was calculated as

$$\Delta E_{subAl(T1Al-T1Ce)} = E_{subAl(T1Al)} - E_{subAl(T1Ce)}$$

where E_{subAl(T1Al)} and E_{subAl(T1Ce)} are the E_{subAl} when T1 site was occupied by Al³⁺ and Ce³⁺ respectively. The higher ΔE_{subAl(T1Al-T1Ce)} corresponds to an easier substitution of Si⁴⁺ by Al³⁺ at NNN T sites.

3. Results and discussion

3.1. Composition and textural properties

The N₂ adsorption-desorption isotherms were recorded to evaluate the porosity of different samples (Fig. 2). According to the IUPAC classification, the xCe-M samples exhibits transformation of isotherms from Type I to a combination of Type I and IV with the increase of Ce content, suggesting that the mesopores are formed by Ce incorporation. The N₂ uptake at P/P₀ < 0.05 indicates that all the samples have microporous structure, and the addition of Ce in the synthesis process does not significantly affect the micropores. The hysteresis loop of the xCe-M is enlarged along with addition of Ce, denoting that these samples have greater external surfaces. The textural properties derived from the N₂ adsorption-desorption isotherm are listed in Table 1. Decreases in micropore surface area and micropore volume with increasing Ce contents in the samples were obtained. This tendency may be attributed to the destruction of the zeolite framework, and/or the occupation of internal space by extra framework species. On the other hand, the mesopore volume and media pore width increase with increasing the Ce content, owing to the creation of structure defects by incorporating Ce ions into the zeolite framework. Compared with 0Ce-M sample, ball milling process (0Ce-M-BM) resulted in a slight decline in micropore surface

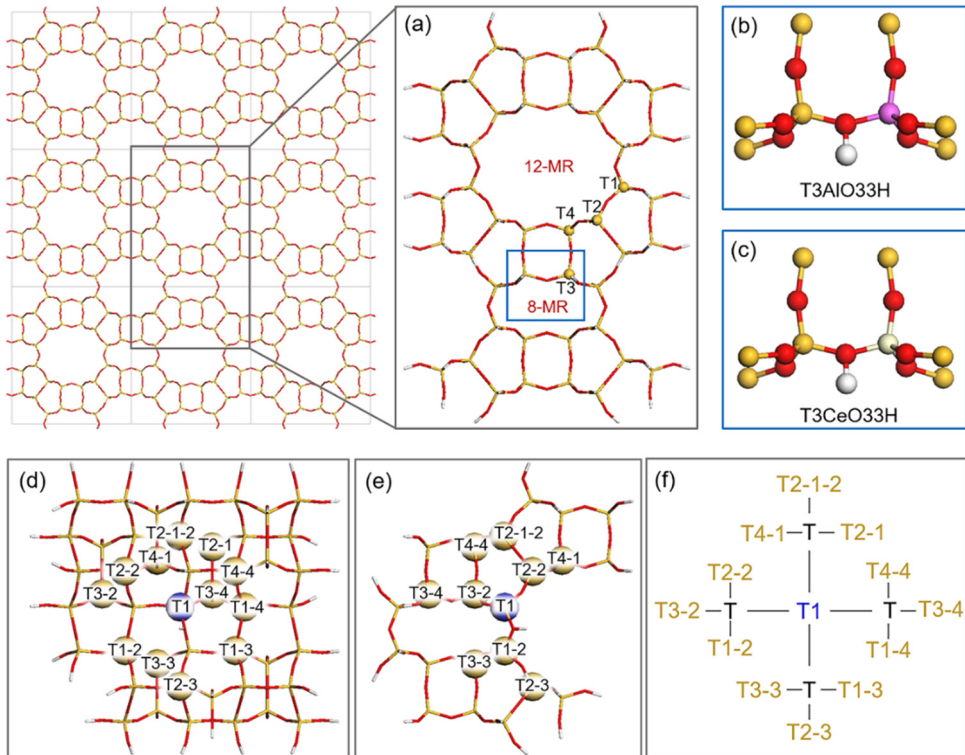


Fig. 1. (a) Structure of studied 100 T MOR model, (b) enlargement of T3AlO₃₃H site in 100 T MOR model, (c) enlargement of T3CeO₃₃H site in 100 T MOR model, (d) side view and (e) front view of studied 62 T structure, and (f) diagram of the labels in 62 T.

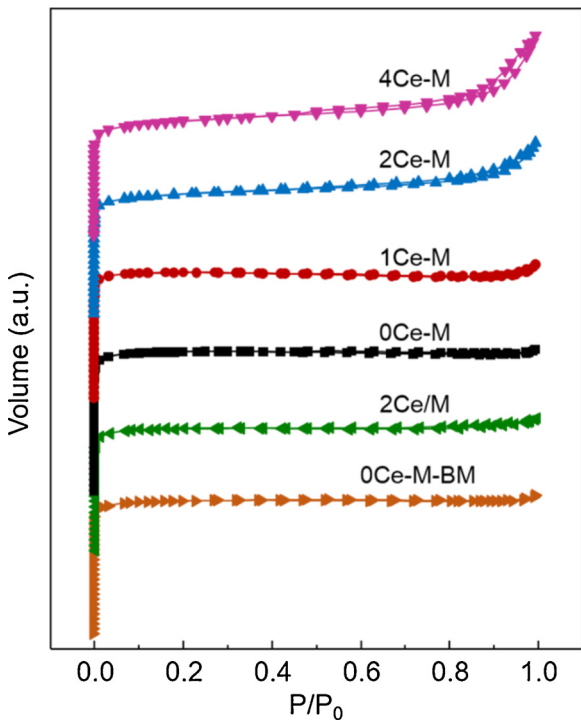


Fig. 2. N₂ adsorption and desorption isotherms of samples.

area, due to partial deterioration of zeolite framework. For the 2Ce/M sample, both the surface area and the pore volume are smaller than those of 0Ce-M-BM, indicative of micropores blocking by CeO_x.

Table 1
The textural properties of samples.

Sample	Pore volume (cm ³ ·g ⁻¹)			Median pore width (nm)	Micropore surface area (m ² ·g ⁻¹)
	Total	Micro-	Meso-		
0Ce-M	0.220	0.203	0.017	0.86	436
1Ce-M	0.207	0.190	0.017	0.86	407
2Ce-M	0.263	0.159	0.104	1.04	333
4Ce-M	0.306	0.143	0.163	1.66	307
2Ce/M	0.195	0.179	0.016	0.87	384
0Ce-M-BM	0.207	0.185	0.022	0.87	402

3.2. Framework incorporation

The element composition of Ce-incorporated MOR zeolites with different Ce contents as well as the mole percentage of Ce in sum of Ce, Al, and Si (M_{Ce}%) are summarized in Table 2. Although the initial Al contents of the raw materials are equivalent in the mixed sol-gel, the actual concentrations of Al and Si in the xCe-M ($x = 0, 1, 2$) samples are found to decrease with increasing Ce concentration, evidencing the inherent competition between framework T atom (Si and Al) and Ce during the hydrothermal synthesis process. However, when the M_{Ce}% reached 4.1%, the amount of both the Al and Si species decrease sharply, which might be caused by the partially collapse of the MOR structure through heteroatoms incorporating into zeolite framework.

Powder XRD was employed to explore the phase composition and refine the unit cell parameters of all samples. Fig. 3a shows the XRD patterns of the xCe-M and ball-milled samples. The typical diffraction peaks associated with MOR zeolites are present for all the xCe-M samples, suggesting that well-crystallized MOR zeolites are obtained in this study. No characteristics of Ce related species are observed, indicative of high dispersion in xCe-M samples. Moreover, one of the strongest peak in the XRD pattern of the MOR zeolite corresponding to the crystal plane of (150) is magnified in Fig. 3b. The peak gradually

Table 2

Chemical composition and unit cell parameters of samples.

Sample	Element content (mmol·g ⁻¹)			$\frac{\text{Ce}}{\text{Ce}+\text{Al}+\text{Si}}\text{ (%)}$	Unit cell parameter			
	Si	Al	Ce		a(Å)	b(Å)	c(Å)	V(Å ³)
0Ce-M	14.20	1.30	0	0	18.13	20.12	7.46	2722
1Ce-M	14.20	1.27	0.18	1.1	18.22	20.10	7.48	2741
2Ce-M	14.08	1.17	0.33	2.1	18.16	20.32	7.49	2762
4Ce-M	9.85	0.75	0.45	4.1	18.15	20.32	7.49	2761
2Ce/M	14.05	1.29	0.33	2.1	18.13	20.22	7.46	2736
0Ce-M-BM	14.12	1.29	0	0	18.15	20.20	7.46	2735

shifts towards smaller angles with increasing M_{Ce}%, which implies an increase in the unit lattice parameters. Since radius of Ce ion is larger than that of Al and Si ions, the unit lattice parameter is increased upon Ce ions incorporation into the framework of MOR [25,34].

Unlike the case of xCe-M samples, 2Ce/M sample prepared by ball milling presents both of the CeO₂ and MOR phases. Given the almost identical Ce content in 2Ce-M and 2Ce/M, it is conclusive that one-pot synthesis makes the Ce species well-dispersed on H-MOR, while physical mixing process results in considerable CeO₂ aggregates, which is supported by TEM images (Fig. S2). The shift in the diffraction peak at $2\theta = 22.3^\circ$ and the variation of unit cell parameter are not observed, suggesting that the substitution effect is not prompted by physical mixing and the variations in the XRD pattern of xCe-M are not caused by CeO₂ species.

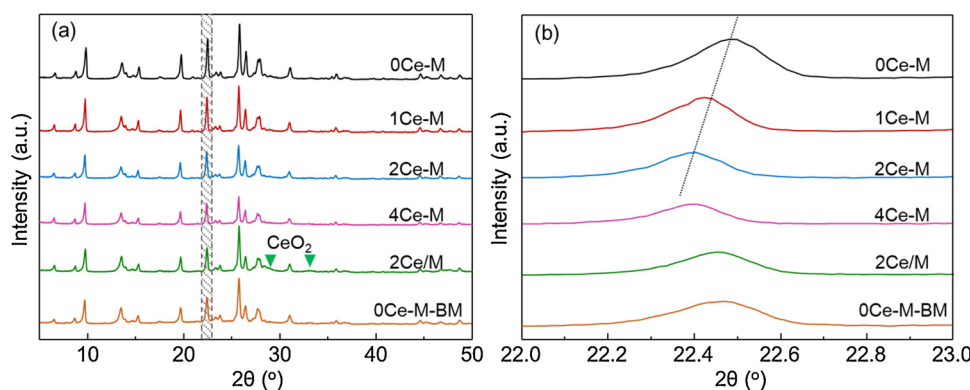
The UV-vis spectra (shown in Fig. 4a) show absorption bands at around 210 nm, attributed to the aluminosilicate matrix [35]. The band at 270 nm, associating with the tetrahedral Ce³⁺ in MOR, becomes more intense as the M_{Ce}% increases [25,36]. In addition, an adsorption band at higher than 320 nm emerges as the major band for 2Ce/M and as a shoulder for xCe-M, indicating the coexistence of extraframework CeO_x nanocrystallites [37]. It is noteworthy that due to the high dispersion of the extraframework species, the CeO₂ phase is not identified in the XRD pattern of the xCe-M samples.

The core level XPS spectrum of the O 1s spectrum pertaining to 0Ce-M shows a main peak at 532.4 eV (Fig. 4b), which is attributed to the binding energy (BE) of oxygen in alumino-silicates. With the increment of Ce, the peak progressively shifts to the higher BE side. Generically, a higher BE value indicates a lower electronegativity of adjacent atoms [38]. Considering that the electronegativity of Ce atom (1.12) is much lower than that of Al atom (1.61), the isomorphous substitution of Al by Ce would increase the electron density of the framework oxygen and result in an increase in BE. However, the O 1s BE of 4Ce-M is identical to that of the 2Ce-M, because it is difficult for excess Ce atoms to incorporate into the MOR framework as the M_{Ce}% is higher than 2.1%. Besides, a shoulder at about 530 eV assigned to the oxygen in the CeO_x lattice arises in 4Ce-M and 2Ce/M, revealing that the unincorporated Ce species are present as CeO₂ in 4Ce-M [39].

The FTIR spectra of Ce-incorporated samples in the region of framework T–O–T vibration exhibit all the characteristic bands of MOR zeolite, similar to the 0Ce-M (Fig. 4c). Nevertheless, the band at 1082 cm⁻¹, due to asymmetric stretching of T–O–T, gradually broadens as the amount of Ce increases, indicating isomorphous substitution by heteroatom in zeolites [40,41]. Notably, the two references (i.e. 2Ce/M and 0Ce-M-BM) also exhibit sharp peak at 1082 cm⁻¹, verifying that the broadening of T–O–T vibration in xCe-M is caused by incorporation of Ce.

As Raman is a sensitive approach to characterize zeolite textures, it is conducted to explore the effect of Ce addition on the MOR framework (Fig. 4d). The well-resolved bands at 395 and 450 cm⁻¹ are assigned to bending mode of 5-membered ring (5-MR) and 4-membered ring (4-MR), respectively [42]. Notably, a red shift of the band at 395 cm⁻¹ is observed upon Ce-incorporated samples, while the other band stays at 450 cm⁻¹. In MOR framework, 5-MR consists of T1, T2 and T4 site, while 4-MR contains T3 and T4 site [43]. Thus, Ce atoms occupy the T1 and T2 site rather than T3 and T4 sites. Besides, the 2Ce/M and 0Ce-M-BM display the similar Raman spectra as 0Ce-M, suggesting that both extraframework CeO_x and ball-milling process show very limited effect on the MOR framework.

The ²⁹Si MAS NMR spectra of 0Ce-M, 2Ce-M, 2Ce/M exhibit four overlapped peaks (Fig. 5). The peaks between -100 ppm and -120 ppm are attributed to Q4 [Si(0 M)] site. The peaks at -105 ppm and -100 ppm are assigned to Q3 [Si(1 M)] and Q2 [Si(2 M)] site, respectively [44]. The peaks of Q2 and Q3 sites in 2Ce-M shift to upfield relative to those of 0Ce-M, indicating that the Ce has successfully incorporated into zeolite framework during one-step hydrothermal process [25,45]. Besides, the positions of Q4 peaks stay at -112.2 ppm and -113.3 ppm for all the samples, that is to say, the chemical environment of Si(0 M) is not influenced by heteroatoms. Note that no peak shift is observed in ball-milled sample (2Ce/M), comparing with 0Ce-M. These observations imply that the CeO_x species do not affect the peak position and confirms that the upfield shift of Q2 and Q3 peaks in 2Ce-M is definitely caused by the Ce incorporation.

Fig. 3. (a) XRD patterns of samples and (b) enlarged scale between $2\theta = 22.0^\circ - 23.0^\circ$.

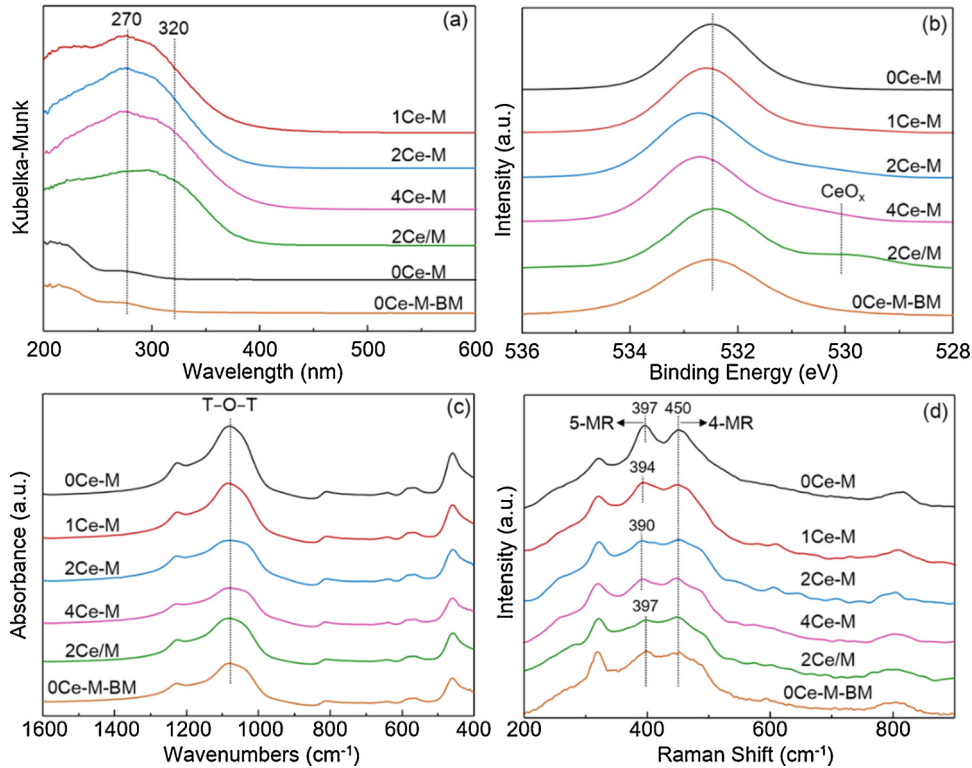


Fig. 4. (a) UV–vis spectra, (b) O 1s XPS spectra, (c) FTIR spectra in the region of framework T–O–T vibration, and (d) Raman spectra of samples.

3.3. Quantification of acid sites in different channels

NH₃-TPD measurements were employed to explore the acidity of zeolite and the corresponding profiles are depicted in Fig. 6a. The TPD curves were deconvoluted into three peaks by Gaussian curves, denoted as P₁, P₂, and P₃. The desorption temperature of P₁, P₂ and P₃ are related to weak, moderate and strong acid sites, respectively. According to previous studies, the desorption peak of P₃ in the high-temperature region is associated with framework Brønsted acid site because it completely disappears when all the framework Brønsted acid sites are replaced by Na⁺ [32,46,47]. The total amount of Brønsted acid sites (B_{total}) of the samples is calculated based on the peak areas of P₃ and the results are listed in Table 3. With increasing M_{Ce}% from 0 to 2.1%, B_{total} increases significantly, suggesting that the Ce replacement is a major contributor to the increase in the number of Brønsted acid sites. It should be mentioned that when the M_{Ce}% reached 4.1%, the B_{total} does not increase any more as a result of the collapse of MOR framework, which has been testified by BET analyses. Furthermore, the peak position of P₃ for the 0Ce-M sample is about 35 °C higher in comparison to that for the Ce-incorporated samples, indicating that Ce incorporation leads to a decrease in acidic strength. On the other hand, comparing the B_{total} of 2Ce/M with 0Ce-M-BM, Ce species do not contribute to Brønsted acid sites. In contrast, Ce addition results in a slight decline in

B_{total}, indicating the number of accessible Brønsted acid sites decreases, possibly owing to the partial blocking of channels by CeO_x species.

We also performed NH₃-adsorption IR to quantify the acidity of different samples. As shown in Fig. 6b, the bands at 1430 cm⁻¹ and 1620 cm⁻¹ are attributed to NH₃ interacted with Brønsted and Lewis acid sites, respectively. The extinction coefficient of 0.11 cm²·μmol⁻¹ for 1430 cm⁻¹ and 0.026 cm²·μmol⁻¹ for 1620 cm⁻¹ are applied to calculate the concentration of acid sites [48]. As listed in Table 3, the amounts of Brønsted acid sites show similar values and same variation trend to the results obtained from NH₃-TPD. On the other hand, the number of Lewis acid sites is maintained at approximate 40 μmol/g with increasing M_{Ce}% from 0 to 2.1%, indicating that the incorporation of Ce shows negligible influence on Lewis acidity. It should be noted that the amounts of Lewis acid sites increase in 4Ce-M and 2Ce/M samples compared with that in xCe-M (x = 0, 1, 2), resulting from excess unsaturated or extra-framework Ce species [49].

The acidity in 12-MR can be selectively measured by pyridine-adsorption IR, due to its suitable molecular kinetic diameter [12]. As shown in Fig. 6c, the bands at 1540 cm⁻¹ and 1630 cm⁻¹ are associated with pyridine adsorbed on Brønsted acid sites while the bands at 1450 cm⁻¹ and 1610 cm⁻¹ are attributed to pyridine associated with Lewis acid sites [50]. The band at 1490 cm⁻¹ is assigned to the overlap between Brønsted and Lewis acid sites. The quantities of Brønsted and

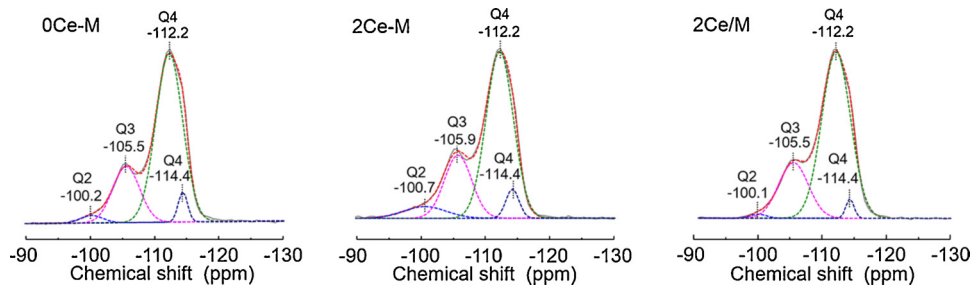


Fig. 5. ²⁹Si MAS NMR spectra of samples.

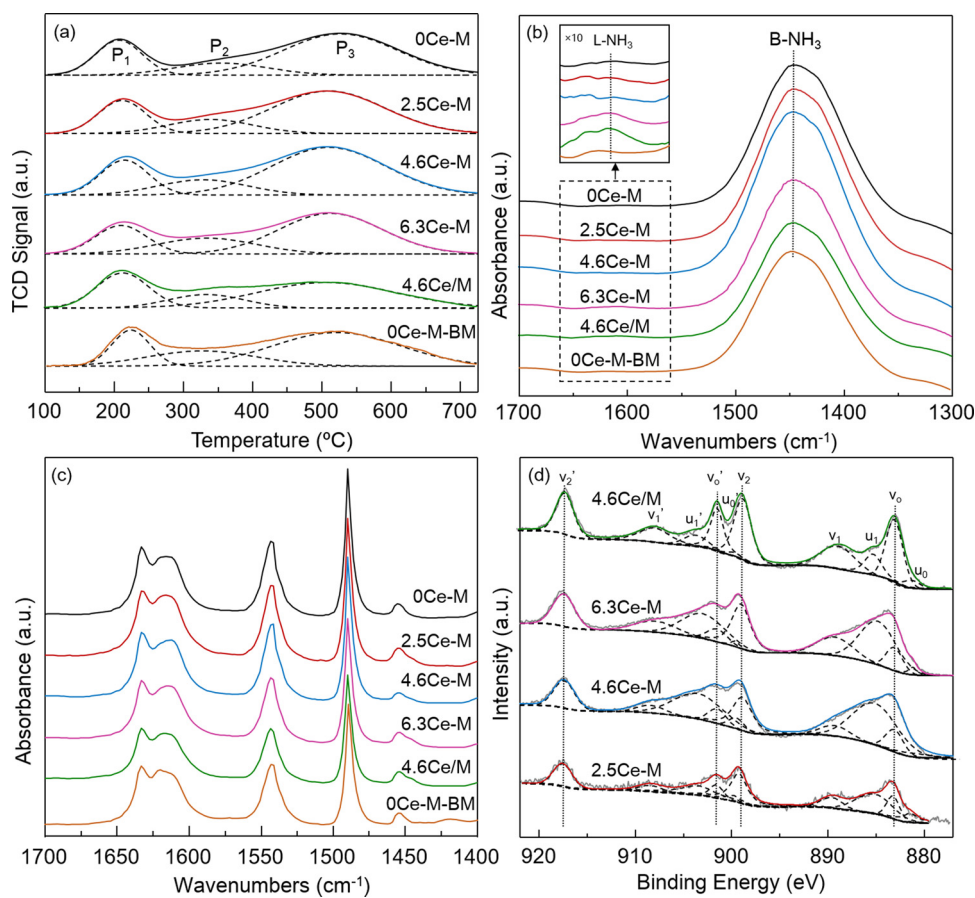


Fig. 6. (a) NH_3 -TPD profiles, (b) NH_3 -adsorption IR spectra, (c) pyridine-IR spectra and (d) Ce 3d XPS spectra of samples.

Lewis acid sites are calculated based on the integrated areas of the band at 1540 cm^{-1} and 1450 cm^{-1} and their molar extinction coefficients ($\epsilon_B = 1.67$ and $\epsilon_L = 2.22\text{ cm}/\mu\text{mol}$, respectively) calculated by Emeis [51]. As summarized in Table 3, all the samples have similar amount of Lewis acid sites in 12-MR. Combined with the results from NH_3 -adsorption IR, it can be inferred that neither Lewis acidity in 8-MR nor that in 12-MR is changed after Ce incorporation for $x\text{Ce-M}$ ($x = 0, 1, 2$). Besides, with increasing the $M_{\text{Ce}}\%$ from 0 to 2.1%, the number of Brønsted acid sites in 12-MR channel ($B_{12\text{-MR}}$) is almost maintained, which is further confirmed by Pyridine-TPD (Fig. S3). Considering the gradual increase of B_{total} and nearly constant L_{total} in these three samples, the incorporated Ce species mainly affect the distribution of Brønsted acid sites in the 8-MR channel.

Table 3
The quantity of framework Al (Al_F) and Ce^{3+} and acidity of samples ($\mu\text{mol g}^{-1}$).

Sample	Quantity of elements			Quantity of acid sites					
	Al_F^{a}	$\text{Ce}^{3+}^{\text{b}}$	$\text{Ce}^{4+}^{\text{b}}$	$B_{\text{total}}^{\text{c}}$	$B_{\text{total}}^{\text{d}}$	$L_{\text{total}}^{\text{d}}$	$B_{12\text{-MR}}^{\text{e}}$	$L_{12\text{-MR}}^{\text{e}}$	$B_{8\text{-MR}}^{\text{f}}$
0Ce-M	1107	0	0	1218	1088	40	416	33	802
1Ce-M	1093	78	98	1289	1170	48	420	42	869
2Ce-M	1035	190	140	1425	1246	48	416	29	1009
4Ce-M	648	199	251	1134	1001	93	355	36	779
2Ce/M	1097	59	269	903	880	122	304	36	599
0Ce-M-BM	1082	0	0	1104	942	44	367	36	737

^a Calculated based on ICP-OES and ^{27}Al MAS NMR.

^b Calculated based on ICP-OES and XPS.

^c Calculated based on NH_3 -TPD.

^d Calculated based on IR spectra of NH_3 adsorption.

^e Calculated based on pyridine adsorption IR.

^f $B_{8\text{-MR}} = B_{\text{total}} \cdot B_{12\text{-MR}}$.

3.4. Exploring the origin of new generated Brønsted acid sites

To provide a more intuitive understanding on the Brønsted acid sites distribution, the proportion of Brønsted acid sites in 8-MR ($B_{8\text{-MR}}\%$) is employed. It is calculated according to the following equation:

$$B_{8\text{-MR}}\% = B_{8\text{-MR}}/B_{\text{total}} * 100\%$$

The calculated proportions of $B_{8\text{-MR}}$ for 0Ce-M and 2Ce-M are 65.8% and 70.8%, respectively, which are consistent with the $B_{8\text{-MR}}\%$ calculated from deconvolution of FTIR spectra of O–H region (Table S1 and Fig. S4). These results confirm that the regulation of Brønsted acid sites distribution is achieved through incorporation of Ce.

XPS was employed to analyze the valence states of Ce ions. As a

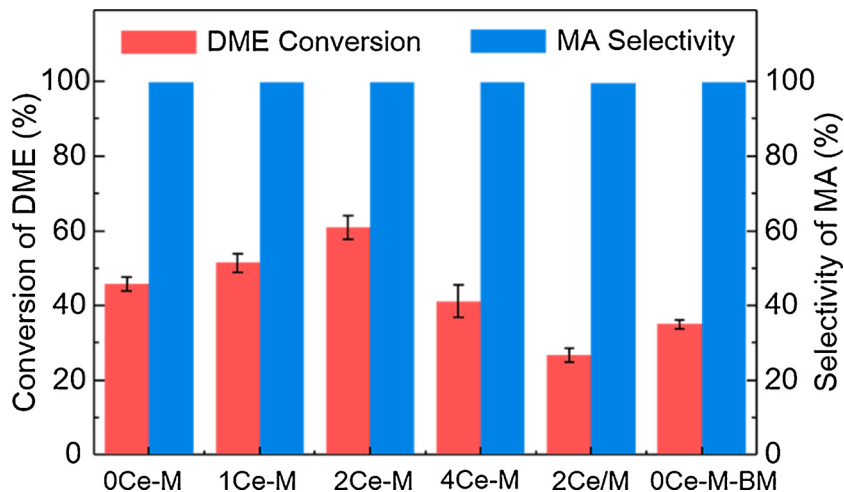


Fig. 7. DME conversion and MA selectivity of DME carbonylation over the catalyst. Reaction conditions: 200 °C, 1.5 MPa, DME/CO = 1/49, 6000 h⁻¹.

consequence of hybridization between the O 2p states and Ce 4f levels, the Ce 3d spectra are complicated [52]. According to literature [53,54], the spectra in Fig. 6d could be deconvoluted into five Ce 3d_{5/2, 3/2} spin-orbit doublet peaks: two doublet for Ce³⁺ and three doublet for Ce⁴⁺. The four peaks for Ce³⁺ are labeled as u₀ (881.1 eV), u₁ (885.0 eV), u_{0'} (899.5 eV) and u_{1'} (903.4 eV). The six characteristic peaks for Ce⁴⁺ are labeled as v₀ (882.8 eV), v₁ (889.4 eV), v₂ (898.7 eV), v_{0'} (901.2 eV), v_{1'} (907.5 eV) and v_{2'} (917.1 eV). The peaks labeled as v or u are associated with 3d_{5/2} photoemissions, while the peaks risen from 3d_{3/2} emission are labeled as v' and u'. The positions of the five peaks were fixed and the integrated peak area ratios of v to v', and u to u' are constrained with the value of 1.5. The decomposition and fitting of the XPS spectra were carried out using the software of XPS Peak Fit. The quantitative data of Ce³⁺ and Ce⁴⁺ amount based on XPS deconvolution and ICP are listed in Table 3. With increasing the M_{Ce}%, the amount of Ce³⁺ and Ce⁴⁺ both increase. Nevertheless, the momentum of Ce³⁺ slows down significantly, when the M_{Ce}% increases from 2.1% to 4.1%. Besides, the ratio of Ce³⁺ to Ce⁴⁺ in 2Ce/M is quite different from the 2Ce-M samples, owing to the difference in Ce species between the two samples.

In the following, we took XPS together with O₂-chemisorption and ICP-OES to quantitatively characterize the different Ce species. Taking 2Ce/M (prepared by ball-milling) as an example, almost all of Ce should exist as extraframework species. The deconvolution of XPS shows more than 80% Ce species are Ce⁴⁺, which indicates CeO₂ is the dominant species after calcination in air at 500 °C. O₂-chemisorption can be used as a powerful tool to quantify Ce³⁺ in CeO_x due to the existence of oxygen vacancy. The result of O₂-chemisorption shows that 51 μmol·g⁻¹ of Ce³⁺ are present as Ce₂O₃ that is almost equal to the total amount of Ce³⁺ (59 μmol·g⁻¹). Therefore, it is conclusive that most of the extraframework CeO_x species in sample are CeO₂, while Ce³⁺ species are present as Ce₂O₃. As neither CeO₂ nor framework Ce⁴⁺ generates Brønsted acid site, we focus on analysis of Ce³⁺ species for one-pot synthesized samples (i.e. xCe-M).

As listed in Table 3, the total amounts of Ce³⁺ in xCe-M (x = 1 and 2) increase with increasing M_{Ce}%. O₂-chemisorption measurement demonstrates that no O₂ consumption is observed on 0Ce-M and there is hardly any Ce₂O₃ species in the other two samples (the amounts of Ce³⁺ in Ce₂O₃ for 1Ce-M and 2Ce-M are 2.3 and 4.7 μmol·g⁻¹ respectively). Considering that the sum of Ce³⁺ and F_{Al} increases proportionally with the B_{total} ($R^2 = 1.000$), it is reasonable to infer that nearly all the Ce³⁺ ions successfully incorporate into MOR framework during hydrothermal crystallization at low M_{Ce}%. Besides, as the Ce³⁺ incorporated into MOR framework is difficult to be reduced, peak at around 570 °C in H₂-TPR profile is considered as the H₂ consumption of the extraframework CeO_x species [55]. The normalized peak area of

xCe-M samples increases with the Ce content (Fig. S5), indicating the existence of more and more CeO_x aggregates. Note that the 2Ce-M obtained by ball-milling exhibits the highest H₂ consumption. These results are in line with the other characterizations such as XPS, UV-vis etc. Moreover, the calculated ratios of framework Ce³⁺ to CeO_x (Ce_F/CeO_x) agree well with the semi-quantified results based on deconvolution of UV-vis spectra (Fig. S6 and Table S2), confirming the above conclusion.

In principle, in aluminosilicate zeolite, the density of Brønsted acid site is in accordance with the concentration of Al_F. However, B_{total} increases by incorporation of Ce in our case, accompanied with a decline in the quantity of Al_F. Note that an increment of Ce³⁺ species is observed along with the increase in B_{total} and the B_{total} is increasing in line with the sum of Al_F and Ce³⁺, which gives a solid evidence that partial Brønsted acid sites originate from the bridging hydroxyl groups of Si—OH—Ce (similar to Si—OH—Al) due to the interaction of tetrahedral Ce³⁺ with Si—O bonds. Thus, we conclude that the distribution of Brønsted acid site is tailored by Ce³⁺ incorporation.

3.5. Catalytic performance of Ce-containing zeolite for DME carbonylation

DME carbonylation catalyzed by MOR has been reported as a typical spatial-confined reaction, in which the rate of MA formation is strictly proportional to the number of Brønsted acid sites within 8-MR channels [32,56,57]. As discussed above, the Brønsted acid sites located in 8-MR are concentrated through Ce incorporation. Thus, we investigated the catalytic performance of Ce-doped MOR catalysts in carbonylation of DME, expecting an improvement in MA yield.

Fig. 7 illustrates the initial activities of the xCe-M, 2Ce/M and 0Ce-M-BM (time on stream = 1.5 h) under the same reaction conditions, and the DME conversion versus time on stream are shown in Fig. S7. All samples exhibit an approximate selectivity greater than 98%, indicating an excellent confinement effect with respect to the 8-MR channels in MOR. An obvious deactivation is observed in all samples due to the coke deposition in 12-MR. The initial DME conversion increases from 45.7% to 61.0% as the M_{Ce}% increases from 0 to 2.1%, owing to the enrichment of Brønsted acid sites within 8-MR channels. Besides, the DME conversion of 2Ce-M is higher than that of 0Ce-M in 7 h, confirming the enhancement of activity caused by Ce-incorporation. Further increasing the M_{Ce}% to 4.1% results in a decreased activity, because of lower concentration of Brønsted acid sites. In addition, the DME conversion of the 0Ce-M-BM is 35.0%, apparently lower than the activity of 0Ce-M, which is due to loss of Brønsted acid sites during ball-milling process. Note that the DME conversion of the 2Ce/M sample is only 26.7%, which can be ascribed to the covering of active sites by

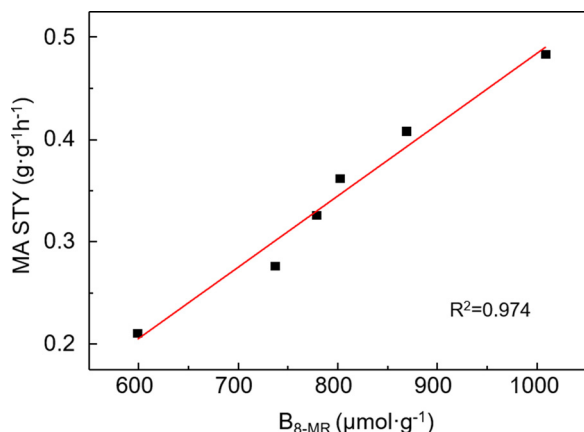


Fig. 8. Correlation between the reactivity of DME carbonylation and the amount of Brønsted acid sites in 8-MR channels.

CeO_x species. For a better presentation of the relationship between activity and active sites, we plotted the STY_{MA} against the amount of Brønsted acid sites within 8-MR (Fig. 8). As expected, a positive linear correlation is observed with $R^2 = 0.974$, confirming that the activity of DME carbonylation is primarily governed by the number of Brønsted acid sites within 8-MR. The comparison of activity between the 2Ce-M and published work are shown in Table S3.

In conclusion, incorporating a proper content of Ce, for instance, with a $M_{\text{Ce}}\%$ of 2.1% in the MOR zeolite allows for the enrichment of Brønsted acid sites within 8-MR, leading to a favorable catalytic performance with respect to the carbonylation of DME.

3.6. Discriminating the active sites for DME carbonylation

The upshot of the above experiments provides some clues: (i) Ce incorporates into MOR framework as Ce^{3+} species, generating new Brønsted acid sites. (ii) enrichment of Brønsted acid sites in 8-MR leads to an enhanced activity for MA formation. (iii) existence of extra-framework CeO_x species causes activity loss because of deterioration of zeolitic structure. From these observations, we infer two possible promotion mechanism of Ce incorporation: a) New Brønsted acid centers in 8-MR that balance the negative charges induced by the framework Ce^{3+} atoms (Si—OH—Ce) in tetrahedral sites function as active sites for the carbonylation of DME. b) Competitive occupancy of Ce^{3+} and Al^{3+} changes the distribution of Al among nonequivalent sites (i.e. 8-MR and 12-MR), enriching the bridging hydroxyl groups related to Al atoms (Si—OH—Al) in 8-MR. In this section, we endeavor to distinguish the two hypothetical promotion mechanisms by computational and experimental study.

Given that the Brønsted acid sites located at T3O33 in 8-MR channels are active for this reaction, we explore the acidic property of Si—OH—Al and Si—OH—Ce on T3O33 by calculating the bond length of O—H ($d(\text{O—H})$) and deprotonation energy (shown in Table 4). Note that a longer $d(\text{O—H})$ and a lower E_{DPE} correspond to greater acid strength. The calculations of all of these parameters suggest that the acidity of H-[Al]-MOR is stronger than that of H-[Ce]-MOR. This trend is in line with the observations from the NH_3 -TPD.

Table 4

The bond length of O—H ($d(\text{O—H})$) and the deprotonation energy (DPE) of Al and Ce substituted MOR at the T3 site in 8-MR, the activation barriers and reaction energies of CO insertion to form acetyl.

Samples	$d(\text{O—H})$ (Å)	DPE (kcal/mol)	Activation Barriers (kcal/mol)	Reaction Energy (kcal/mol)
T3AlO33H	0.980	310.2	27.6	-13.0
T3CeO33H	0.975	316.4	37.9	-2.4

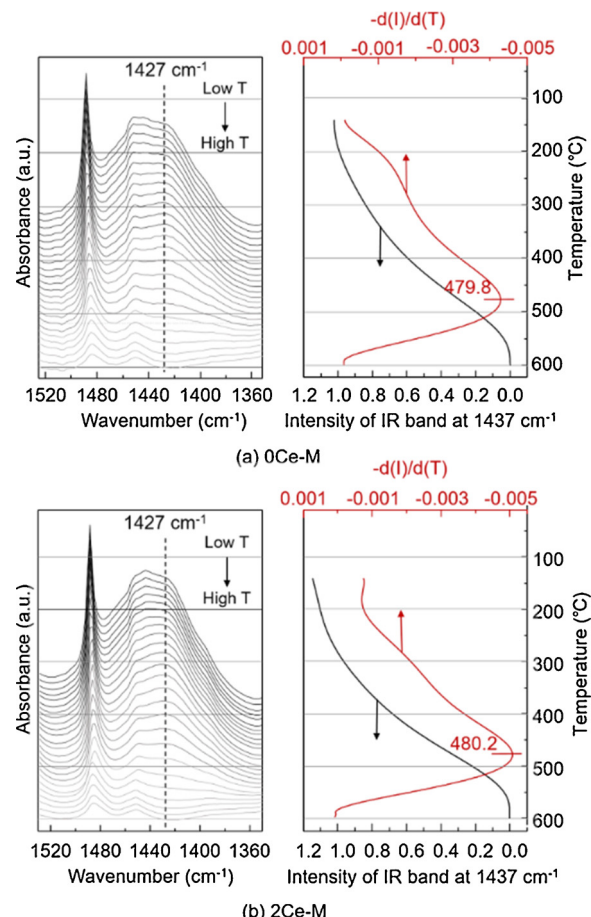


Fig. 9. IR-TPD of NH_3 on the (a) 0Ce-M and (b) 2Ce-M.

Although the overall properties of Brønsted acid sites in MOR have been detected by the NH_3 molecules, the information of Brønsted acid site in 8-MR is difficult to be distinguished from NH_3 -TPD profiles. Thus, in order to explore the acidity of Brønsted in 8-MR, we performed IR-TPD of NH_3 on the pyridine saturated MOR, in which the Brønsted acid site in 12-MR were selectively blocked by pyridine. When the pyridine saturated samples expose to NH_3 atmosphere at 150°C , a band at 1427 cm^{-1} emerges that is ascribed to the NH_3 molecule adsorbed on Brønsted acid site. Since the Brønsted acid sites in 12-MR have been poisoned by pyridine molecules, this band can be considered as a characteristic of the Brønsted acid site in 8-MR. With increasing the temperature from 150°C to 600°C under vacuum condition, the intensity of the band at 1427 cm^{-1} decreases due to the desorption of NH_3 on Brønsted acid site in 8-MR [58]. The desorption rate of NH_3 (r_{NH_3}) is calculated by $r_{\text{NH}_3} = -\frac{d(I)}{dT}$, in which the I is measured from the intensity of the band at 1427 cm^{-1} . As shown in Fig. 9, the temperatures at the desorption rate maximum of 0Ce-M and 2Ce-M are identical, indicating that the acid strength in 8-MR keeps constant even after Ce incorporation into the framework of MOR. As we mentioned above, DFT calculations reveal that the acidic strength of Si—OH—Ce is weaker than that of Si—OH—Al. Taking these observations together, we can conclude the protons in 8-MR of 2Ce-M balance the negatively charged framework induced by the presence of tetrahedrally coordinated Al^{3+} rather than Ce^{3+} , which are similar to the Brønsted acid sites in 0Ce-M.

In the mechanism of DME carbonylation, CO insertion into CH_3 to form acetyl has been identified as the rate limiting step [10]. Herein, we calculated the energy barrier for rate limiting step to explore the catalytic ability of H-[Al]-MOR and H-[Ce]-MOR. The activation barriers are 27.6 kcal/mol and 37.9 kcal/mol for H-[Al]-MOR and H-[Ce]-MOR, respectively. This indicates that the reaction occurring on a Brønsted

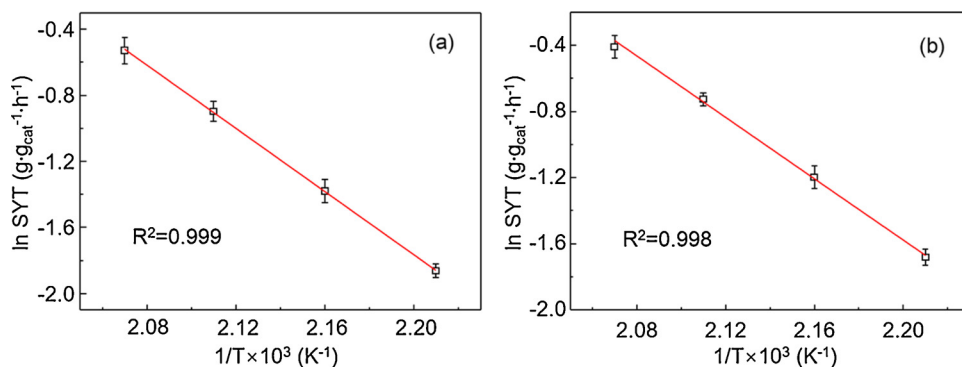


Fig. 10. Kinetic plot of the DME carbonylation catalyzed by 0Ce-M (a) and 2Ce-M (b) based on the Arrhenius equation.

acid site generated by Al is easier than that on a proton associated with Ce. On the other hand, DFT calculations show that acetyl formation is exothermic for both types of Brønsted acid sites, with a reaction energy of -2.4 kcal/mol for H-[Ce]-MOR and -13.0 kcal/mol for H-[Al]-MOR. This signifies that the configuration of acetyl adsorbed on H-[Al]-MOR is more stable than that on H-[Ce]-MOR. The results also suggest that a weak Brønsted acid is less active than a comparably stronger acid site [59].

Fig. 10 displays the temperature dependence of the reactivity of the DME carbonylation in the form of Arrhenius plots, which was obtained on the basis of the space time yield of MA at various temperatures (180°C , 190°C , 200°C and 210°C). As Brønsted acid sites in 12-MR are responsible for the coke formation, the initial STY on the fresh catalyst is employed to eliminate the influence of coke. The calculated apparent activation energies for the 0Ce-M and 2Ce-M catalysts are 19.0 kcal/mol and 18.2 kcal/mol , respectively. We also calculated the TOFs of 0Ce-M and 2Ce-M, and the results are 6.1 h^{-1} and 6.4 h^{-1} , respectively. The similarity in apparent activation energy and TOF are indicative of identical active sites for both catalysts.

In summary, comparing the experimental results with DFT calculations, we confirm that Brønsted acid sites in the 8-MR of 2Ce-M samples is also generated by Al^{3+} rather than Ce^{3+} . In other words, the new generated Brønsted acid sites (Si-OH-Ce) does not function as active sites for the carbonylation of DME and the superior activity of 2Ce-M is attributed to the enrichment of Si-OH-Al in 8-MR through Ce incorporation (Table 5).

3.7. Mechanistic understanding about the enrichment of Si-OH-Al in the 8-MR

In order to shed light on the mechanism of changes in Brønsted acid sites distribution in different channels, we calculated the preferred tetrahedral site for Al or Ce atom among four T sites of MOR. The

Table 5

The E_{sub} of Al at different site when T1 site has been occupied by Ce^{3+} or Al^{3+} (kJ/mol).

Site	$E_{\text{subAl(T1Al)}}$	$E_{\text{subAl(T1Ce)}}$	$\Delta E_{\text{subAl(T1Al-T1Ce)}}$
T2-1	-122.2	-127.5	5.5
T4-1	-160.7	-172.5	11.8
T2-1-2	-141.4	-139.2	-2.2
T2-2	-149.6	-168.2	18.6
T3-2	-116.1	-145.6	29.5
T1-2	-179.2	-188.7	9.5
T2-3	-146.3	-128.6	-17.7
T1-3	-148.7	-155.9	7.2
T3-3	-160.8	-181.3	20.5
T1-4	-124.8	-131.9	7.1
T3-4	-158.0	-176.7	18.7
T4-4	-132.5	-136.3	3.8

relative energies of Ce^{3+} and Al^{3+} substitution in the MOR structure are shown in Table S4. The results show that both of the Ce^{3+} and Al^{3+} prefer to locate at the T1 site, consistent with the previous studies [17,60]. These results also coincide with the observations on Raman spectra that the Ce-incorporation influences the T-O-T vibration of 5-MR (T1, T2 and T4) while it does not affect the T-O-T vibration of 4-MR (T3 and T4).

To clarify the effect of Ce-incorporation on Al distribution, we set two models that T1 sites have been occupied by Ce^{3+} and Al^{3+} , respectively, and calculated the substitution energies of the second Al^{3+} at next-nearest-neighbor (NNN) T-sites of T1 on these two models ($E_{\text{subAl(T1Ce)}}$ for Ce^{3+} substituted model and $E_{\text{subAl(T1Al)}}$ for Al^{3+} substituted model, respectively). According to the E_{subAl} difference ($\Delta E_{\text{subAl(T1Al-T1Ce)}}$) on these two models, Ce^{3+} located at T1 site leads to the easier substitution of the second Al^{3+} at most of NNN T-sites, as evidenced by $\Delta E_{\text{subAl(T1Al-T1Ce)}} > 0$ except for T2-1-2 and T2-3 sites. Furthermore, among the NNN T sites of T1, T3 sites (i.e. T3-2, T3-3, T3-4, all in 8-MR) show the highest $\Delta E_{\text{subAl(T1Al-T1Ce)}}$. In other words, the occupancy of Al^{3+} on T3 sites is most significantly influenced by Ce incorporation, which results in an enrichment of Brønsted acid sites in 8-MR.

4. Conclusion

In summary, we successfully synthesized a series of Ce-incorporated MOR zeolites by employing a facile one-step hydrothermal route. Comparing with the ball-milling counterpart, incorporation of Ce atoms into zeolitic framework has been evidenced by multiple characterization techniques, such as lattice expansion in XRD patterns, characteristic peak of tetrahedral Ce^{3+} in UV-vis, peak shifts of O1 s XPS, Raman, ^{29}Si MAS NMR and broadening framework T-O-T vibrations in IR, NH_3 -TPD, IR spectra of NH_3 adsorption and XPS results demonstrated that Ce located at T sites in MOR as Ce^{3+} species, which created new Brønsted acid sites. The quantitative analysis of Brønsted acid sites validated that the distribution of Brønsted acid sites in the different channels (8-MR and 12-MR) of H-MOR are modulated by Ce incorporation. Incorporating a proper content of Ce, for instance, with a $M_{\text{Ce}}\%$ of 2.1% in the MOR zeolite, is able to enrich the Brønsted acid sites in the 8-MR, whereas the number of Brønsted acid sites in 12-MR are kept unchanged. An established linear correlation between the amount of $B_{8\text{-MR}}$ and STY_{MA} indicates that the increase of the $B_{8\text{-MR}}$ caused by Ce isomorphous substitution is responsible for the promoted catalytic activity in DME carbonylation. Typically, a STY_{MA} of $0.483 \text{ gg}^{-1} \cdot \text{h}^{-1}$ can be achieved at 200°C , which is 32.6% higher than that on 0Ce-M. Besides, the 0Ce-M and 2Ce-M exhibit almost identical Brønsted acid strength in 8-MR and the apparent active energy for DME carbonylation reaction. Since Si-OH-Al and Si-OH-Ce have distinct acidity that governs corresponding activation barrier, we attributed the improvement in activity to the enrichment of Si-OH-Al group within the 8-MR structures. Furthermore, DFT calculation revealed that

incorporation of Ce influences the occupancy of Al on T3 site significantly, which contributes to the enrichment effect on Brønsted acid sites in 8-MR. This study provides a facile approach to regulate the acidity of zeolites (not only strength but also distribution), which contributes to developing zeolite catalysts for various reactions.

Notes

The authors declare no competing financial interest.

Acknowledgements

We gratefully acknowledge the financial support from the National Natural Science Foundation of China (21325626, 21406120) and the Program of Introducing Talents of Discipline to Universities (B06006). We thank Horiba Co. for the Raman measurement.

Appendix A. Supplementary data

Supplementary material related to this article can be found, in the online version, at doi:<https://doi.org/10.1016/j.apcatb.2019.117777>.

References

- [1] J. Goldemberg, Ethanol for a sustainable energy future, *Science* 315 (2007) 808–810.
- [2] H. Yue, X. Ma, J. Gong, An alternative synthetic approach for efficient catalytic conversion of syngas to ethanol, *Acc. Chem. Res.* 47 (2014) 1483–1492.
- [3] Y. Amao, N. Shuto, H. Iwakuni, Ethanol synthesis based on the photoredox system consisting of photosensitizer and dehydrogenases, *Appl. Catal. B: Environ.* 180 (2016) 403–407.
- [4] Q. Wei, G. Yang, X. Gao, L. Tan, P. Ai, P. Zhang, P. Lu, Y. Yoneyama, N. Tsubaki, A facile ethanol fuel synthesis from dimethyl ether and syngas over tandem combination of Cu-doped HZSM35 with Cu-Zn-Al catalyst, *Chem. Eng. J.* 316 (2017) 832–841.
- [5] X. Li, X. San, Y. Zhang, T. Ichii, M. Meng, Y. Tan, N. Tsubaki, Direct synthesis of ethanol from dimethyl ether and syngas over combined H-Mordenite and Cu/ZnO catalysts, *ChemSusChem* 3 (2010) 1192–1199.
- [6] G. Yang, X. San, N. Jiang, Y. Tanaka, X. Li, Q. Jin, K. Tao, F. Meng, N. Tsubaki, A new method of ethanol synthesis from dimethyl ether and syngas in a sequential dual bed reactor with the modified zeolite and Cu/ZnO catalysts, *Catal. Today* 164 (2011) 425–428.
- [7] P. Lu, G. Yang, Y. Tanaka, N. Tsubaki, Ethanol direct synthesis from dimethyl ether and syngas on the combination of noble metal impregnated zeolite with Cu/ZnO catalyst, *Catal. Today* 232 (2014) 22–26.
- [8] H. Shen, Y. Li, S. Huang, K. Cai, Z. Cheng, J. Lv, X. Ma, The carbonylation of dimethyl ether catalyzed by supported heteropoly acids: the role of Brønsted acid properties, *Catal. Today* (2018), <https://doi.org/10.1016/j.cattod.2018.04.001>.
- [9] G.G. Volkova, L.M. Plyasova, A.N. Salanov, G.N. Kustova, T.M. Yurieva, V.A. Likholobov, Heterogeneous catalysts for halide-free carbonylation of dimethyl ether, *Catal. Lett.* 80 (2002) 175–179.
- [10] P. Cheung, A. Bhan, G.J. Sunley, E. Iglesia, Selective carbonylation of dimethyl ether to methyl acetate catalyzed by acidic zeolites, *Angew. Chem. Int. Ed.* 45 (2006) 1617–1620.
- [11] A. Bhan, A.D. Allian, G.J. Sunley, D.J. Law, E. Iglesia, Specificity of sites within eight-membered ring zeolite channels for carbonylation of methyls to acetyls, *J. Am. Chem. Soc.* 129 (2007) 4919–4924.
- [12] T. He, X. Liu, S. Xu, X. Han, X. Pan, G. Hou, X. Bao, Role of 12-ring channels of mordenite in DME carbonylation investigated by solid-state NMR, *J. Phys. Chem. C* 120 (2016) 22526–22531.
- [13] A.A.C. Reule, J.A. Sawada, N. Semagina, Effect of selective 4-membered ring dealumination on mordenite-catalyzed dimethyl ether carbonylation, *J. Catal.* 349 (2017) 98–109.
- [14] M. Maache, A. Janin, J.C. Lavalle, E. Benazzi, FT infrared study of Brønsted acidity of H-mordenites: heterogeneity and effect of dealumination, *Zeolites* 15 (1995) 507–516.
- [15] M. Boronat, C. Martinez-Sanchez, D. Law, A. Corma, Enzyme-like specificity in zeolites: a unique site position in mordenite for selective carbonylation of methanol and dimethyl ether with CO, *J. Am. Chem. Soc.* 130 (2008) 16316–16323.
- [16] Z. Cheng, S. Huang, Y. Li, J. Lv, K. Cai, X. Ma, Deactivation kinetics for the carbonylation of dimethyl ether to methyl acetate on H-MOR, *Ind. Eng. Chem. Res.* 56 (2017) 13618–13627.
- [17] Y. Li, Q. Sun, S. Huang, Z. Cheng, K. Cai, J. Lv, X. Ma, Dimethyl ether carbonylation over pyridine-modified MOR: enhanced stability influenced by acidity, *Catal. Today* 311 (2018) 81–88.
- [18] Z. Ristanovic, J.P. Hofmann, G. De Cremer, A.V. Kubarev, M. Rohnke, F. Meirer, J. Hofkens, M.B.J. Roeflaers, B.M. Weckhuysen, Quantitative 3D fluorescence imaging of single catalytic turnovers reveals spatiotemporal gradients in reactivity of zeolite H-ZSM-5 crystals upon steaming, *J. Am. Chem. Soc.* 137 (2015) 6559–6568.
- [19] M. Silaghi, C. Chizallet, P. Raybaud, Challenges on molecular aspects of dealumination and desilication of zeolites, *Microporous Mesoporous Mater.* 191 (2014) 82–96.
- [20] V. Machado, J. Rocha, A.P. Carvalho, A. Martins, Modification of MCM-22 zeolite through sequential post-synthesis treatments. Implications on the acidic and catalytic behaviour, *Appl. Catal. A Gen.* 445 (2012) 329–338.
- [21] A.B. Pinar, C. Marquez-Alvarez, M. Grande-Casas, J. Perez-Priente, Template-controlled acidity and catalytic activity of ferrierite crystals, *J. Catal.* 263 (2009) 258–265.
- [22] Y. Román-Leshkov, M. Moliner, M.E. Davis, Impact of controlling the site distribution of Al atoms on catalytic properties in ferrierite-type zeolites, *J. Phys. Chem. C* 115 (2011) 1096–1102.
- [23] A. Janda, A.T. Bell, Effects of Si/Al ratio on the distribution of framework Al and on the rates of alkane monomolecular cracking and dehydrogenation in H-MFI, *J. Am. Chem. Soc.* 135 (2013) 19193–19207.
- [24] A. Ikhlaq, B. Kasprzyk-Hordern, Catalytic ozonation of chlorinated VOCs on ZSM-5 zeolites and alumina: formation of chlorides, *Appl. Catal. B: Environ.* 200 (2017) 274–282.
- [25] Y. Wu, J. Wang, P. Liu, W. Zhang, J. Gu, X. Wang, Framework-substituted lanthanide MCM-22 zeolite: synthesis and characterization, *J. Am. Chem. Soc.* 132 (2010) 17989–17991.
- [26] Y. Liu, L. Xu, L. Zhao, L. Wei, X. Liu, Z. Yan, Substituting effect of Ce³⁺ on the AlPO-11 molecular sieve, *Catal. Sci. Technol.* 11 (2016) 3821–3831.
- [27] C. Hammond, N. Dimitratos, J.A. Lopez-Sanchez, R.L. Jenkins, G. Whiting, S.A. Kondrat, M.H. ab Rahim, M.M. Forde, A. Thetford, H. Hagen, E.E. Stangland, J.M. Moulijn, S.H. Taylor, D.J. Wilcock, G.J. Hutchings, Aqueous-phase methane oxidation over Fe-MFI zeolites: promotion through isomorphous framework substitution, *ACS Catal.* 3 (2013) 1835–1844.
- [28] M.A. Sanhoob, O. Muraza, E.N. Shafei, T. Yokoi, K.-H. Choi, Steam catalytic cracking of heavy naphtha (C12) to high octane naphtha over B-MFI zeolite, *Appl. Catal. B: Environ.* 210 (2017) 432–443.
- [29] A. Ghorbanpour, J.D. Rimer, L.C. Grabow, Computational assessment of the dominant factors governing the mechanism of methanol dehydration over H-ZSM-5 with heterogeneous aluminum distribution, *ACS Catal.* 6 (2016) 2287–2298.
- [30] A.J. Jones, R.T. Carr, S.I. Zones, E. Iglesia, Acid strength and solvation in catalysis by MFI zeolites and effects of the identity, concentration and location of framework heteroatoms, *J. Catal.* 312 (2014) 58–68.
- [31] H. Zhan, S. Huang, Y. Li, J. Lv, S. Wang, X. Ma, Elucidating the nature and role of Cu species in enhanced catalytic carbonylation of dimethyl ether over Cu/H-MOR, *Catal. Sci. Technol.* 5 (2015) 4378–4389.
- [32] M. Wang, S. Huang, J. Lv, Z. Cheng, Y. Li, S. Wang, X. Ma, Modifying the acidity of H-MOR and its catalytic carbonylation of dimethyl ether, *Chin. J. Catal.* 37 (2016) 1530–1537.
- [33] M. Niwa, S. Nishikawa, N. Katada, IRMS-TPD of ammonia for characterization of acid site in β-zeolite, *Microporous Mesoporous Mater.* 82 (2005) 105–112.
- [34] B. Kalita, A.K. Talukdar, Synthesis and characterization of Ce doped MFI zeolite, *Mater. Chem. Phys.* 133 (2012) 713–717.
- [35] V.S. Gomez, L. Lerici, C. Saux, A.L. Perez, C.D. Brondino, L. Pierella, L. Pizzio, Fe/ZSM-11 as a novel and efficient photocatalyst to degrade Dichlorvos on water solutions, *Appl. Catal. B: Environ.* 202 (2017) 580–586.
- [36] S. Devika, M. Palanichamy, V. Murugesan, Selective oxidation of diphenylmethane to benzophenone over CeAlPO-5 molecular sieves, *Chin. J. Catal.* 33 (2012) 1086–1094.
- [37] T. Ye, W. Huang, L. Zeng, M. Li, J. Shi, CeO₂-platelet from monometallic cerium layered double hydroxides and its photocatalytic reduction of CO₂, *Appl. Catal. B: Environ.* 210 (2017) 141–148.
- [38] I. Grohmann, W. Pilz, G. Walther, H. Kosslick, V.A. Tuan, XPS-investigation of titanium modified MFI-type zeolites, *Surf. Interface Anal.* 22 (1994) 403–406.
- [39] W. Yang, C. Li, H. Wang, X. Li, W. Zhang, H. Li, Cobalt doped ceria for abundant storage of surface active oxygen and efficient elemental mercury oxidation in coal combustion flue gas, *Appl. Catal. B: Environ.* 239 (2018) 233–244.
- [40] H. Zhou, W. Zhu, L. Shi, H. Liu, S. Liu, S. Xu, Y. Ni, Y. Liu, L. Li, Z. Liu, Promotion effect of Fe in mordenite zeolite on carbonylation of dimethyl ether to methyl acetate, *Catal. Sci. Technol.* 5 (2015) 1961–1968.
- [41] Y. Meng, H.C. Genuino, C.H. Kuo, H. Huang, S.Y. Chen, L. Zhang, A. Rossi, S.L. Suib, One-step hydrothermal synthesis of manganese-containing MFI-type zeolite, Mn-ZSM-5, characterization, and catalytic oxidation of hydrocarbons, *J. Am. Chem. Soc.* 135 (2013) 8594–8605.
- [42] Y. Yu, G. Xiong, C. Li, F. Xiao, Characterization of aluminosilicate zeolites by UV Raman spectroscopy, *Microporous Mesoporous Mater.* 46 (2001) 23–34.
- [43] L. Benco, T. Bucko, J. Hafner, H. Toulhoat, Periodic DFT calculations of the stability of Al/Si substitutions and extraframework Zn²⁺ cations in mordenite and reaction pathway for the dissociation of H₂ and CH₄, *J. Phys. Chem. B* 109 (2005) 20361–20369.
- [44] S. Huang, X. Liu, L. Yu, S. Miao, Z. Liu, S. Zhang, S. Xie, L. Xu, Preparation of hierarchical mordenite zeolites by sequential steaming-acid leaching-alkaline treatment, *Microporous Mesoporous Mater.* 191 (2014) 18–26.
- [45] S.J. Kim, K.D. Jung, O.S. Joo, Synthesis and characterization of gallosilicate molecular sieve with the MCM-22 framework topology, *J. Porous Mat.* 11 (2004) 211–218.
- [46] S. Liu, J. Ren, S. Zhu, H. Zhang, E. Lv, J. Xu, Y. Li, Synthesis and characterization of the Fe-substituted ZSM-22 zeolite catalyst with high n-dodecane isomerization performance, *J. Catal.* 330 (2015) 485–496.
- [47] Y. Liu, N. Zhao, H. Xian, Q. Cheng, Y. Tan, N. Tsubaki, X. Li, Facilely synthesized h-

- mordenite nanosheet assembly for carbonylation of dimethyl ether, *ACS Appl. Mater. Inter.* 7 (2015) 8398–8403.
- [48] C.J. Van Oers, K. Góra-Marek, K. Sadowska, M. Mertens, V. Meynen, J. Datka, P. Cool, In situ IR spectroscopic study to reveal the impact of the synthesis conditions of zeolite β nanoparticles on the acidic properties of the resulting zeolite, *Chem. Eng. J.* 237 (2014) 372–379.
- [49] M.W. Schreiber, C.P. Plaisance, M. Baumgartl, K. Reuter, A. Jentys, R. Bermejo-Deval, J.A. Lercher, Lewis-Bronsted acid pairs in Ga/H-ZSM-5 to catalyze dehydrogenation of light alkanes, *J. Am. Chem. Soc.* 140 (2018) 4849–4859.
- [50] S. Huang, Y. Wang, Z. Wang, B. Yan, S. Wang, J. Gong, X. Ma, Cu-doped zeolites for catalytic oxidative carbonylation: the role of Bronsted acids, *Appl. Catal. A Gen.* 417 (2012) 236–242.
- [51] C.A. Emeis, Determination of integrated molar extinction coefficients for infrared absorption bands of pyridine adsorbed on solid acid catalysts, *J. Catal.* 141 (1993) 347–354.
- [52] P. Gaudina, S. Dorge, H. Noualia, D. Kehrlib, L. Michelin, L. Josiena, P. Fioux, L. Vidal, M. Soulard, M. Vierling, M. Molière, J. Patarina, Synthesis of Cu-Ce-KIT-6 materials for SO_x removal, *Appl. Catal. A Gen.* 504 (2015) 110–118.
- [53] C. Anandan, P. Bera, XPS studies on the interaction of CeO₂ with silicon in magnetron sputtered CeO₂ thin films on Si and Si₃N₄ substrates, *Appl. Surf. Sci.* 283 (2013) 297–303.
- [54] M. Li, A.C. van Veen, Tuning the catalytic performance of Ni-catalysed dry reforming of methane and carbon deposition via Ni-CeO_{2-x} interaction, *Appl. Catal. B: Environ.* 237 (2018) 641–648.
- [55] S. Damyanova, B. Pawelec, R. Palcheva, Y. Karakirova, M.C.C. Sanchez, G. Tyuliev, E. Gaigneaux, J.L.G. Fierro, Structure and surface properties of ceria-modified Ni-based catalysts for hydrogen production, *Appl. Catal. B: Environ.* 225 (2018) 340–353.
- [56] P. Cheung, A. Bhan, G. Sunley, D. Law, E. Iglesia, Site requirements and elementary steps in dimethyl ether carbonylation catalyzed by acidic zeolites, *J. Catal.* 245 (2007) 110–123.
- [57] B. Li, J. Xu, B. Han, X. Wang, G. Qi, Z. Zhang, C. Wang, F. Deng, Insight into dimethyl ether carbonylation reaction over mordenite zeolite from in-situ solid-state NMR spectroscopy, *J. Phys. Chem. C* 117 (2013) 5840–5847.
- [58] K. Suzuki, T. Noda, N. Katada, M. Niwa, IRMS-TPD of ammonia: direct and individual measurement of Bronsted acidity in zeolites and its relationship with the catalytic cracking activity, *J. Catal.* 250 (2007) 151–160.
- [59] K. Cai, S. Huang, Y. Li, Z. Cheng, J. Lv, X. Ma, Influence of acid strength on the reactivity of dimethyl ether carbonylation over H-MOR, *ACS Sustain. Chem. Eng.* 7 (2019) 2027–2034.
- [60] T. Demuth, J. Hafner, L. Benco, H. Toulhoat, Structural and acidic properties of mordenite. An ab initio density-functional study, *J. Phys. Chem. B* 104 (2000) 4593–4607.